USE OF SPHERICAL HARMONIC DECONVOLUTION METHODS TO COMPENSATE FOR NON-LINEAR GRADIENT EFFECTS ON MRI IMAGES

Andrew Janke, Huawei Zhao, Gary J. Cowin, Graham J. Galloway and David M. Doddrell.

Centre for Magnetic Resonance, The University of Queensland, St. Lucia Qld 4072, Australia.

Address for correspondence:

Andrew L Janke

Centre for Magnetic Resonance

The University of Queensland

St. Lucia, Qld 4072

Australia

Email Andrew.Janke@cmr.uq.edu.au

Abstract

Spatial encoding in MR techniques is achieved by sampling the signal as a function of time in the presence of a magnetic field gradient. The gradients are assumed to generate a linear magnetic field gradient; typical image reconstruction relies upon this approximation. However, high-speed gradients in the current generation of MRI scanners often sacrifice linearity for consequent speed improvements. Such non-linearity results in distorted images. A presentation of the problem from first principles and a correction method based on a gradient field spherical harmonic expansion is proposed. In our case, the amount of distortion measured within a typical field of view required for head imaging is sufficiently large that without some distortion correction technique, images would be of limited use for stereotaxy or longitudinal studies where precise volumetric information is required.

Words: 4061

Key words: MRI, Gradient, Distortion correction

Running head: Correction of image distortions using spherical harmonic expansion.

List of Symbols:

r	bold r
k	bold k
ρ	rho (Greek)
$\not\gamma$	gamma bar (Greek)
ξ	xi (Greek)
Γ	upper-gamma (Greek)
η	eta (Greek)
θ	theta (Greek)
ϕ	phi (Greek)

Introduction

The quality of a magnetic resonance image is dependent upon the accuracy by which physical position is spatially encoded. As MRI data is now used routinely for stereotaxy, longitudinal studies of atrophy and functional studies, ensuring images have no distortion and inhomogeneity is critical. The principal machine dependant sources of this inhomogeneity are eddy currents, gradient non-linearity, B_0- and B_1 inhomogeneity (18). Here, we present an analytical approach to calculating and removing the effects of non-linear gradients only. The primary reason for a gradient only solution is the recent interest in short-bore high-speed gradients. Although peripheral nerve stimulation is a limiting feature of short rise times, such gradients have found use in high-speed echo planar imaging (EPI) of the heart and diffusion tensor imaging of the brain. To achieve short rise times and avoid peripheral nerve stimulation, designers have restricted the length and limited the number of turns in gradients. These constraints, although suitable for the implementation of pulse sequences having the desired speed, have the undesired consequence of increased non-linearity.

Non-linear pulsed field gradients induce image distortions due to incorrect spatial encoding of the signal. If we assume field gradients are linear, it follows that k-space is sampled linearly and thus the FFT is suitable for reconstruction. However, any deviation from linearity in the gradients results in non-linear data sampling and subsequent errors in image spatial encoding. A non-linear Fourier transformation would allow this data to be correctly transformed to an image. Unfortunately, non-linear Fourier transformation greatly increases computation time by $N/\log_2 N$, relative to a FFT, making real-time image generation computationally prohibitive. Here, we present a general analytical solution to correct image distortions induced by gradient non-linearity. The method is applicable to any gradient configuration. It is robust and more importantly; is based upon an approach where the FFT is maintained for image reconstruction.

The notion of mapping and correcting such MRI distortions is not new; two early papers by Schad et al (15, 16) discuss “pincushion” effects seen with 2D phantoms. Subsequent schemes include using a stereotaxic frame as a reference marker (11, 14), comparing phantom images from CT and MRI (7, 19) and imaging specific MRI phantoms (1, 13, 18, 17) that typically consist of an array of tubes filled with a suitable contrast agent. A later Mizowaki et al paper (12) alludes to an important problem with phantom studies; after assessing the reproducibility of their own phantom based correction, the authors conclude that such correction may be only applicable in limited situations. Field mapping is another approach to determining distortion via induced phase shift (2, 3, 5). Other correction schemes have

been proposed for particular problems including a method for correcting distortions induced when using bi-planar gradients (10). Regardless, these approaches are of limited use in attempting to discern, model or correct distortion due to part of the MRI system in isolation (eg the gradients).

In a recent paper (9) a method has been suggested for the correction of both the intensity variations and geometric distortions induced by non-linear gradients based on treating gradient coils as either an opposed Helmoltz pair for the Z-gradient and a Golay arrangement for the transverse gradients. However, this approach treats the non-linear component of the gradient field as a constant for the intensity correction and demonstrates correction of the non-linear induced distortion by correcting a large phantom (a cube of approximately 20cm length). It is also assumed that for the chosen gradient geometry only second order terms are important. Whilst this approach is useful for gradients with a significant length to diameter ratio (>2), it is of limited use with current high-speed gradients with significant higher order gradient field impurities.

In a recent patent (8) it has been suggested that spherical harmonics may be useful in developing a general robust method, but none is given. Another patent application (20) has suggested a method to reconstruct k-space based upon an assumed non-linearity; the method proposed involves approximately 10^{14} triple integrations and thus is of limited practical value. Nevertheless, this patent application does strike at the heart of the problem; any method, which is of practical value, must use the FFT as its basis.

Theory

In MRI, image $\mathbf{r} = (x, y, z)$ and $\mathbf{k} = (k_x, k_y, k_z)$ space is connected by a Fourier transformation. During a pulse sequence, magnetic field gradients play the crucial role of generating k-space coverage. The signal from a single rf excitation of the whole sample in the presence of a set of three orthogonal gradients may be written as the Fourier transform

$$s(\mathbf{k}) = \int \rho(\mathbf{r}) e^{-i2\pi \mathbf{k}\cdot\mathbf{r}} d^3 r \qquad [1]$$

Here, $s(\mathbf{k})$ is the signal in k-space and $\rho(\mathbf{r})$ is the spin density in image space. The reconstructed image, $\hat{\rho}(\mathbf{r})$, is the inverse Fourier transform of the measured data, $s_m(\mathbf{k})$

$$\hat{\rho}(\mathbf{r}) = \int s_m(\mathbf{k}) e^{i2\pi \mathbf{k}\cdot\mathbf{r}} d^3 k \qquad [2]$$

The three implicitly time dependent components of **k** are related to the respective gradient-

component integrals

$$k_x = \gamma \int^t G_x(\mathbf{r},t')dt' \ , \ k_y = \gamma \int^t G_y(\mathbf{r},t')dt' \ , \ k_z = \gamma \int^t G_z(\mathbf{r},t')dt' \qquad [3]$$

Here, γ is a constant and (G_x, G_y, G_z) are the gradient components. The gradient field is a function (non-linear) of the position vector $\mathbf{r} = (x, y, z)$. In standard MR imaging, k-space is sampled at a single time rate and under the assumption that linear gradient fields are applied. If the gradient field is non-linear, there will be a geometric distortion of these images. Knowing the exact gradient field profiles is the key to solving this problem.

Accurately describing the gradient field distribution is not a simple task. The most general approach is to expand the field using spherical harmonics as the basis function (6). The field B_Z generated by a gradient field (V = X, Y, or Z, respectively) can be written in spherical coordinates as follows where $B_{V(n,m)}(r,\theta,\phi)$ is a spherical harmonics expansion of order *n* and degree *m* of each component of the gradient field, and has the form:

$$B_{V(n,m)}(r,\theta,\phi) = r^n \left[a_{V(n,m)} \cos(m\phi) + b_{V(n,m)} \sin(m\phi) \right] P_{(n,m)}(\cos\theta) \qquad [4]$$

where $a_{V(n,m)}$ and $b_{V(n,m)}$ are constants, ***r*** is the radial distance from the magnet isocentre. The associated Legendre functions are $P_{(n,m)}(\cos\theta)$. With a finite number of terms, the summation of the equation [4] is only an approximation of the true gradient field B_Z. The use of spherical harmonics deconvolution to describe magnetic field impurities has been described previously (6). In general, a multi-plane sampling of the DSV (diameter of the spherical volume) is performed in order to ensure over-sampling and accurate estimation of the required gradient impurities. Magnets are usually mapped with up to 24 planes yielding harmonics to the 23rd order. Depending on the gradient set and the design parameters employed, gradient impurities can extend to 7th order requiring at least an 8-plane plot. Even gradient coils from the same manufacturer will have winding errors and thus variation from the predicted field such that it would be inaccurate to use a theoretical field expansion. The optimum method is to measure the actual field strength produced by a particular gradient coil set at a finite number of points in the image space. From this sampling, a function can be constructed to accurately describe the field distribution.

Once knowledge of the gradient field $B_Z(\mathbf{r})$ is established, it can be defined as

$$G_{\mathrm{V}}(\mathbf{r}) \equiv \frac{\partial Bz_{\mathrm{V}}(\mathbf{r})}{\partial v} \equiv \frac{\partial Bz_{\mathrm{V}}^{\mathrm{L}}(v)}{\partial v} + \frac{\partial Bz_{\mathrm{V}}^{\mathrm{N}}(\mathbf{r})}{\partial v} \equiv G_{\mathrm{V}}^{\mathrm{L}} + G_{\mathrm{V}}^{\mathrm{N}}(\mathbf{r}) \qquad [5]$$

Where the subscript *v* is used to denote a spatial dimension (*x*, *y*, or *z*), Bz_{V} is the total gradient field that is generated by a particular coil component, $Bz_{\mathrm{V}}^{\mathrm{L}}$ is the linear gradient field that has only the desired first order harmonic (*v*), and $Bz_{\mathrm{V}}^{\mathrm{N}}$ is the non-linear gradient field defined by the higher order harmonics. For convenience, the subscript *z* will be dropped from $\mathrm{B_z}$ in the following discussion. The gradient $G_{\mathrm{V}}(\mathbf{r})$ contains the following linear ($\mathrm{G_v}$) [6] and non-linear ($\mathrm{B_v}$) components [7]

$$\left(G_{\mathrm{X}}^{\mathrm{L}} = a_{\mathrm{X}(1,1)}, \quad G_{\mathrm{Y}}^{\mathrm{L}} = b_{\mathrm{Y}(1,1)}, \quad G_{\mathrm{Z}}^{\mathrm{L}} = a_{\mathrm{Z}(1,0)} \right) \qquad [6]$$

$$\begin{cases} B_{\mathrm{X}}^{\mathrm{N}}(r,\theta,\phi) = B_{\mathrm{X}(1,0)}(r,\theta,\phi) + \sum_{n=2}\sum_{m} B_{\mathrm{X}(n,m)}(r,\theta,\phi) \\ B_{\mathrm{Y}}^{\mathrm{N}}(r,\theta,\phi) = B_{\mathrm{Y}(1,0)}(r,\theta,\phi) + \sum_{n=2}\sum_{m} B_{\mathrm{Y}(n,m)}(r,\theta,\phi) \\ B_{\mathrm{Z}}^{\mathrm{N}}(r,\theta,\phi) = B_{\mathrm{Z}(1,1)}(r,\theta,\phi) + \sum_{n=2}\sum_{m} B_{\mathrm{Z}(n,m)}(r,\theta,\phi) \end{cases} \qquad [7]$$

By employing the following notation:

$$\begin{cases} \eta_{\mathrm{X}}(x,y,z) = \dfrac{B_{\mathrm{X}}^{\mathrm{N}}(r,\theta,\phi)}{G_{\mathrm{X}}^{\mathrm{L}}} \\ \eta_{\mathrm{Y}}(x,y,z) = \dfrac{B_{\mathrm{Y}}^{\mathrm{N}}(r,\theta,\phi)}{G_{\mathrm{Y}}^{\mathrm{L}}} \\ \eta_{\mathrm{Z}}(x,y,z) = \dfrac{B_{\mathrm{Z}}^{\mathrm{N}}(r,\theta,\phi)}{G_{\mathrm{Z}}^{\mathrm{L}}} \end{cases} \qquad [8]$$

where

$$\begin{cases} r = \sqrt{x^2 + y^2 + z^2} \\ \theta = \tan^{-1}\left(\dfrac{\sqrt{x^2 + y^2}}{z} \right) \\ \phi = \tan^{-1}\left(\dfrac{y}{x} \right) \end{cases} \qquad [9]$$

the mapping from the distorted to undistorted image space can be written as

$$\begin{cases} x' = x - \eta_{\mathrm{X}}(x', y', z') \\ y' = y - \eta_{\mathrm{Y}}(x', y', z') \\ z' = z - \eta_{\mathrm{Z}}(x', y', z') \end{cases} \quad [10]$$

where for the first iteration, the initial values of (x', y', z') are (x, y, z). Equation [10] can thus be solved iteratively for (x', y', z') via the following process.

$$\begin{cases} x'_1 = x - \eta_{\mathrm{X}}(x, y, z) \\ y'_1 = y - \eta_{\mathrm{Y}}(x, y, z) \\ z'_1 = z - \eta_{\mathrm{Z}}(x, y, z) \end{cases}, \begin{cases} x'_2 = x - \eta_{\mathrm{X}}(x'_1, y'_1, z'_1) \\ y'_2 = y - \eta_{\mathrm{Y}}(x'_1, y'_1, z'_1) \\ z'_2 = z - \eta_{\mathrm{Z}}(x'_1, y'_1, z'_1) \end{cases}, \cdots, \begin{cases} x'_n = x - \eta_{\mathrm{X}}(x'_{n-1}, y'_{n-1}, z'_{n-1}) \\ y'_n = y - \eta_{\mathrm{Y}}(x'_{n-1}, y'_{n-1}, z'_{n-1}) \\ z'_n = z - \eta_{\mathrm{Z}}(x'_{n-1}, y'_{n-1}, z'_{n-1}) \end{cases} \quad [11]$$

The convergence of each iteration can be measured by the term:

$$E(n) = \frac{\sqrt{(x'_n - x'_{n-1})^2 + (y'_n - y'_{n-1})^2 + (z'_n - z'_{n-1})^2}}{\sqrt{(x'_n - x)^2 + (y'_n - y)^2 + (z'_n - z)^2}} \quad [12]$$

When the change in this term from subsequent iterations drops below a critical tolerance, iteration stops. In our experience a value of 0.01 was sufficient, and equates to 2.94(0.0058) and 2.72(0.0053) mean (stddev) iterations respectively for a 5th and 7th order discrete solution.

This process does not correct for intensity variations arising from a non-linear gradient field nor does it yield voxels having identical geometric dimensions. Clearly for this method to be useful in data analysis, the voxel dimensions in 3D data have to be geometrically equal (i.e. an image is required at a regular set of points $(l_{\mathrm{X}'}\Delta x', l_{\mathrm{Y}'}\Delta y', l_{\mathrm{Z}'}\Delta z')$). The following operations can be applied to correct the geometric distortion:

$$\begin{cases} x_{l_{\mathrm{X}}} = m_{\mathrm{X}'}\Delta x' + \eta_{\mathrm{X}}(m_{\mathrm{X}'}\Delta x', m_{\mathrm{Y}'}\Delta y', m_{\mathrm{Z}'}\Delta z') \\ y_{l_{\mathrm{Y}}} = m_{\mathrm{Y}'}\Delta y' + \eta_{\mathrm{Y}}(m_{\mathrm{X}'}\Delta x', m_{\mathrm{Y}'}\Delta y', m_{\mathrm{Z}'}\Delta z') \\ z_{l_{\mathrm{Z}}} = m_{\mathrm{Z}'}\Delta z' + \eta_{\mathrm{Z}}(m_{\mathrm{X}'}\Delta x', m_{\mathrm{Y}'}\Delta y', m_{\mathrm{Z}'}\Delta z') \end{cases} \quad [13]$$

From this point, a simple non-linear mass preserving resampling of image data using a discrete solution to the deformations expressed in equation [13] is required as per Langlois et al (9). This method can be readily applied irrespective of the particular pulse sequence and/or k-space trajectory.

Method

We performed a 24-plane spherical harmonic deconvolution NMR plot on a set of high-speed Sonata gradients manufactured by Siemens Aktiengesellschaft, Germany. These gradients are interfaced to an Oxford Magnet Technology 4T whole body magnet. In order to measure the field distribution of the gradients in isolation, the base passively shimmed magnet was plotted first followed by two more plots in which a constant current was applied to the X and Z gradients respectively. By subtracting the base plot from a plot with a gradient energised, the effect of an individual gradient can be obtained. For simplicity, it was assumed that the X and Y gradient distortions were identical. In order to speed correction a discrete solution expressed as a grid function of vectors over an area of interest (+/- 120mm from the isocentre in x, y and z) with a regular spacing of 5mm is generated from the set of spherical harmonic coefficients. Each vector in the volume is generated by iterating towards the solution using the method described in the previous section at each point in the grid and storing the resultant delta values.

This set of deformation vectors can then be applied to any data set within its coverage of space. The time taken to non-linearly resample a 256^3 image using this approach is ~20minutes using average computing hardware (RISC 300Mhz), the generation of the 5mm 3D field only takes on the order of seconds. It is important to note that mass preservation resampling can be easily achieved using the above discrete technique via simple multiplication of the Jacobian determinant plus one of the deformation field as part of the resampling. This type of resampling is often termed “mass-preservation resampling”.

Two imaging experiments were then performed, the first using a phantom for reference purposes to previous work and the second of the human head. The phantom was manufactured by Bruker Medical and is shown in Figure 1. The phantom consists of a cylinder having perfectly flat ends, with a diameter of 18.5cm and depth 3cm. Within the phantom are points marking known distances (20mm for the main grid). Imaging was performed at 1.5T using a turbo spin echo sequence with a 256x256 mm field of view (matrix size 512x512). The slice thickness was set at 5mm and TR was set at 500ms and TE at 25ms. The phantom was imaged in the YZ plane of the magnet.

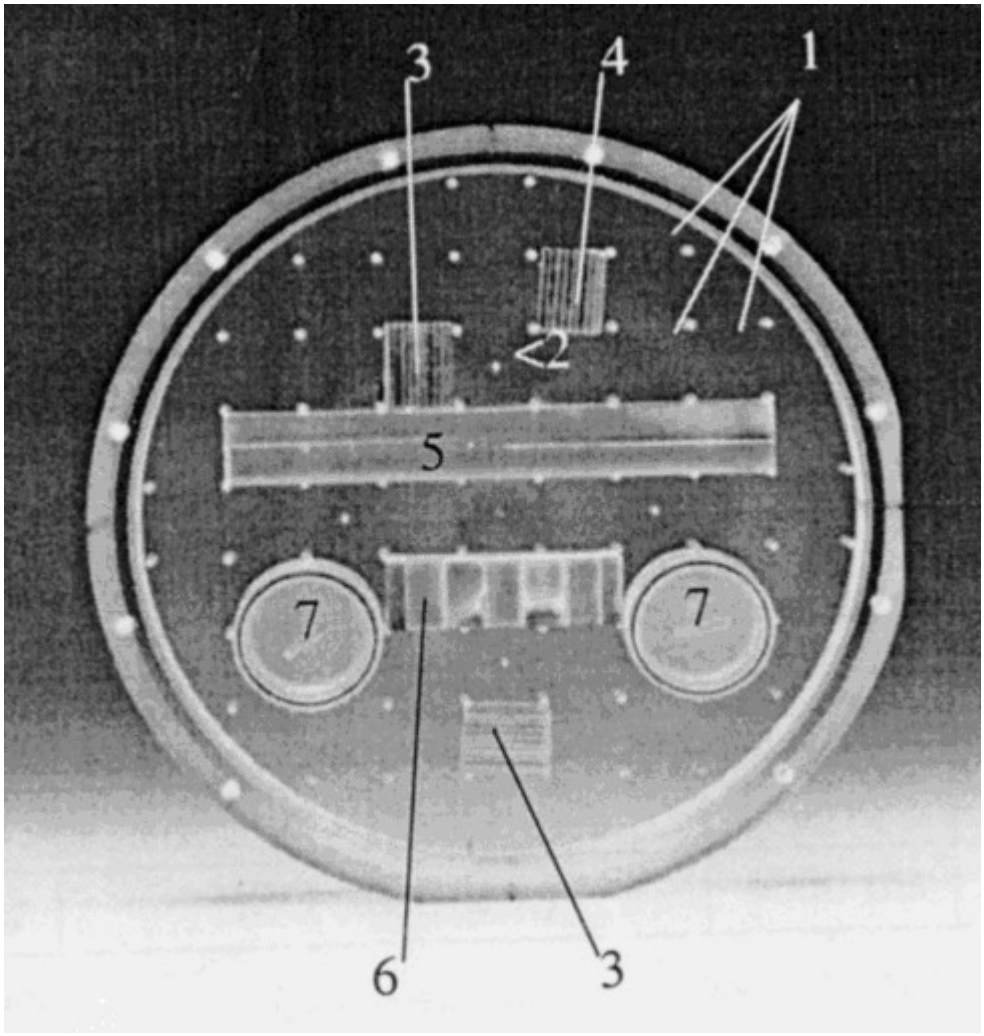

Figure 1 - The Bruker phantom used in this study. The grid markers are shown at 1 and can be seen throughout the phantom. The other markers are quality control for various pulse sequences.

The phantom was imaged a number of times at fixed distances along the X, Y, and Z-axes to give pseudo 3D coverage of the entire of the DSV of the gradients.

To demonstrate the correction techniques effectiveness on more conventional data, two 3D MPRAGE T1 images were acquired at 4T (TR 2.5s TE 3.93ms, TI 1100ms 240mm FOV, matrix size 256x256x256, TEM head coil) of a normal volunteer. The first was acquired with the head coil at the isocentre of the gradients, the second shifted 15mm in the positive z direction.

Results

The plotted spherical harmonics to the 7th order for the gradients are shown in Table 1. The experimental magnetic field distributions for the *X*, *Y*, and *Z* gradients are shown in Figure 2. It is clear from these isomagnetic plots that the gradients produce inhomogeneous magnetic fields and it is likely that image distortion will result.

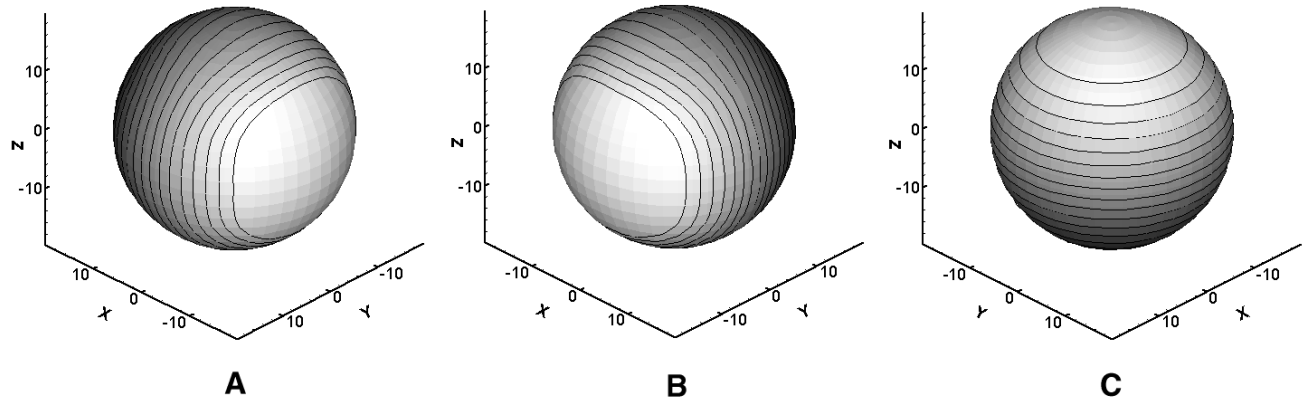

Figure 2 - The magnetic field distribution on a sphere, at a radius of 18cm, for a Sonata gradient set: (a) X-gradient field; (b) Y-gradient field is same as X but 90o rotated; (c) Z-gradient field.

In order to visualise the results it is useful to introduce the following parameter. For any gradient field, the quality of the linear gradient component can be measured by

$$\Gamma(\mathbf{r}') = \frac{G_{\mathrm{V}}^{\mathrm{N}}(\mathbf{r}')}{G_{\mathrm{V}}^{\mathrm{L}}}, \quad \|\mathbf{r}'\| \le r_{dsv} \qquad [14]$$

Here, r_{dsv} is the radius of the DSV. The non-linearity of the gradient field increases with the image volume to such an extent that the effective DSV in our case has a radius of less than 10cm. (As shown below, the effective imaging space is best described by an elliptical volume). Figure 3 demonstrates that the non-linear behaviour increases with the displacement from the isocentre.

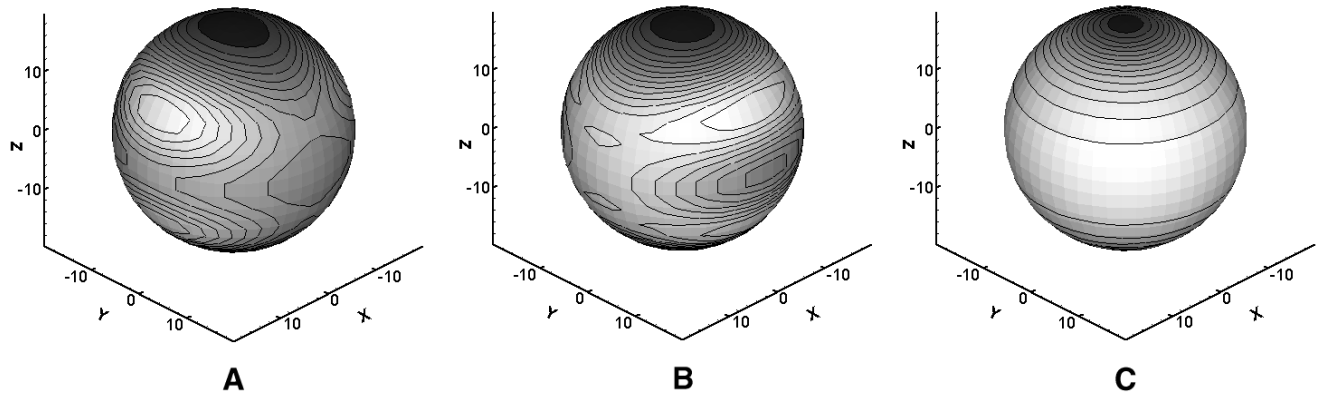

Figure 3 - Plots of the quality function Γ on a sphere (radius 18cm) using the harmonics listed in Table 1. (a) X-gradient. (b) Y-gradient. (c) Z-gradient.

Figure 4(a) shows a 2D image of the phantom sliced in the XY plane with the centre of the phantom placed at the magnet isocentre. Note that the grid markers are visible when this phantom is imaged. A red circle has been superimposed on this image to demonstrate distortions.

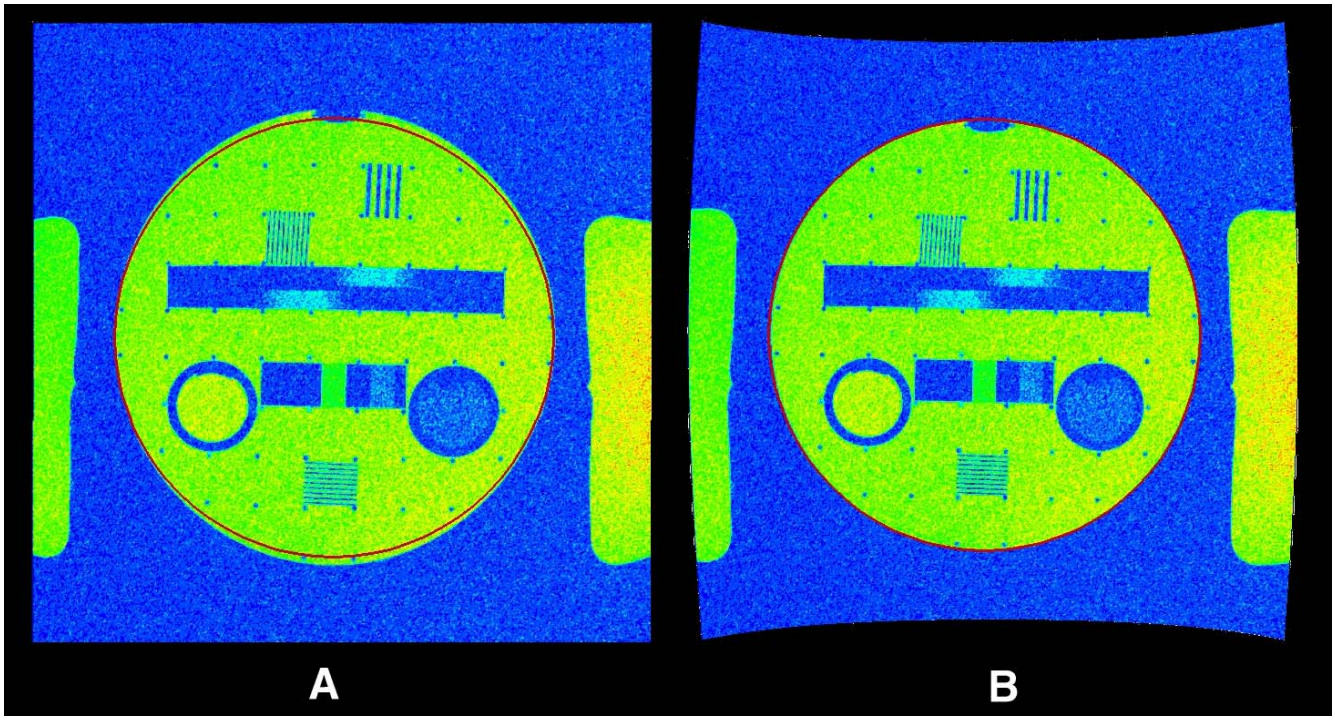

Figure 4 - The phantom centre is at the centre of the imaging domain. The original (a) and corrected (b) images are shown.

The image has been corrected using the harmonics to the 5^{th} order listed in the Table 1. The resultant image is shown in Figure 4(b). The background of the image has also been corrected illustrating that the non-linear properties of the gradients increases for points further removed from the magnet isocentre.

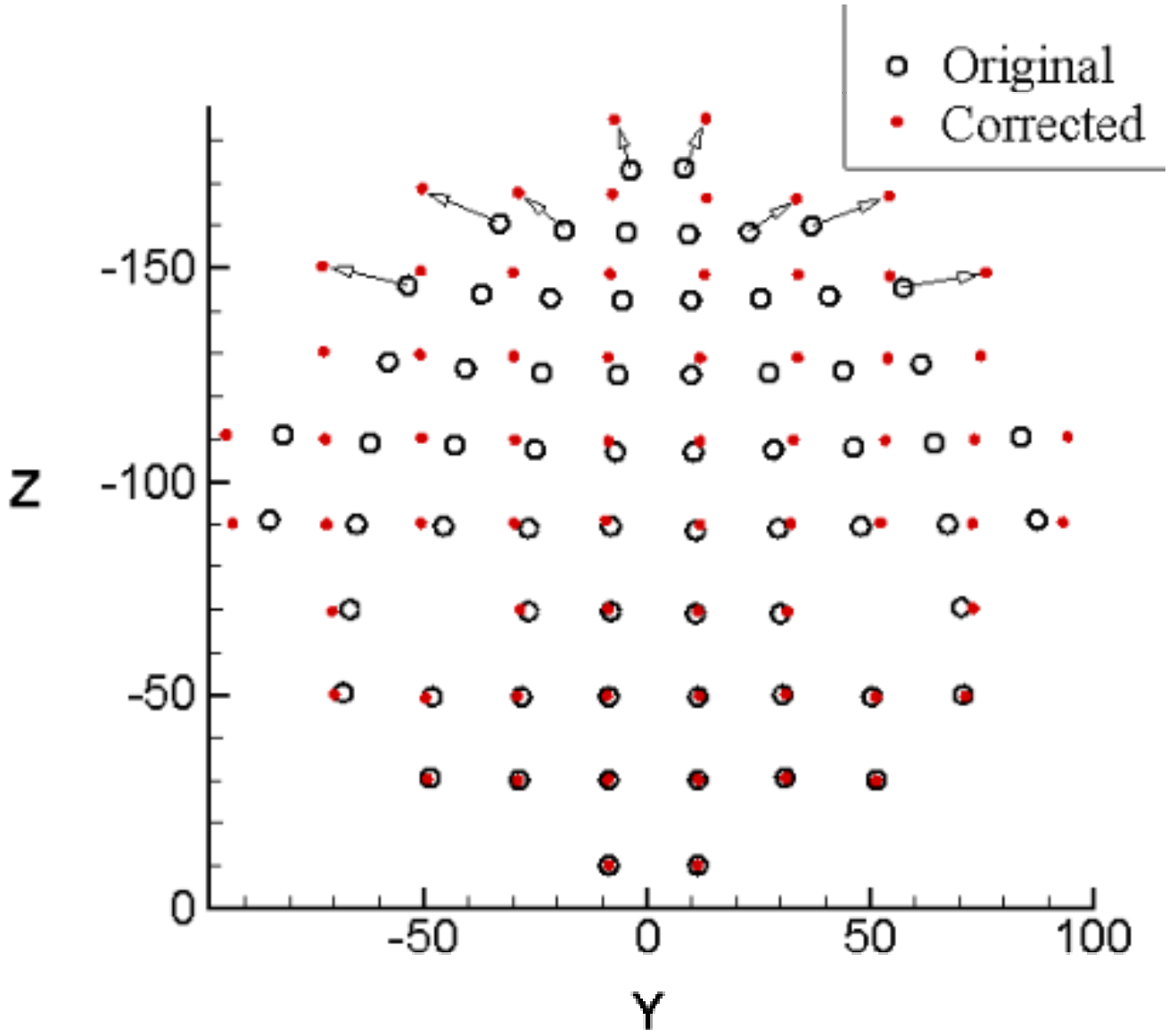

Figure 5 - Spatial positions of the grid points measured in the YZ plane using the Bruker phantom. The open circles are measured and red dots corrected positions. Dimensions are in mm.

To examine part of the non-linearity in a similar fashion to previous phantom studies that use control points, Figure 5 shows the grid positions of the phantom when imaged in the YZ plane with its centre 100mm from the isocentre in Z. The open circles show the imaged position of the grid markers and the red dots their respective corrected positions.

In order to demonstrate the qualitative effects of the correction scheme on anatomic data; both the 0mm (isocentre) and 15mm (plus 15mm in Z plane) images individual geometric distortions were corrected using a discrete non-linear grid transform. To show the effect of the correction scheme with varying levels of complexity the volumes were resampled using grid transforms generated from the spherical harmonic coefficients to the 3^{rd}, 4^{th}, 5^{th}, 6^{th} and 7^{th} orders. Mass preservation resampling was

employed during the interpolation phase. The corrected image volumes were then registered using a rigid body transformation (4) and a voxel difference map calculated. Once both volumes are corrected and registered, rigid structures (eg the cortex) should be identical. An axial slice from each of the corrected 3D volumes and its associated difference images are shown in Figure 6.

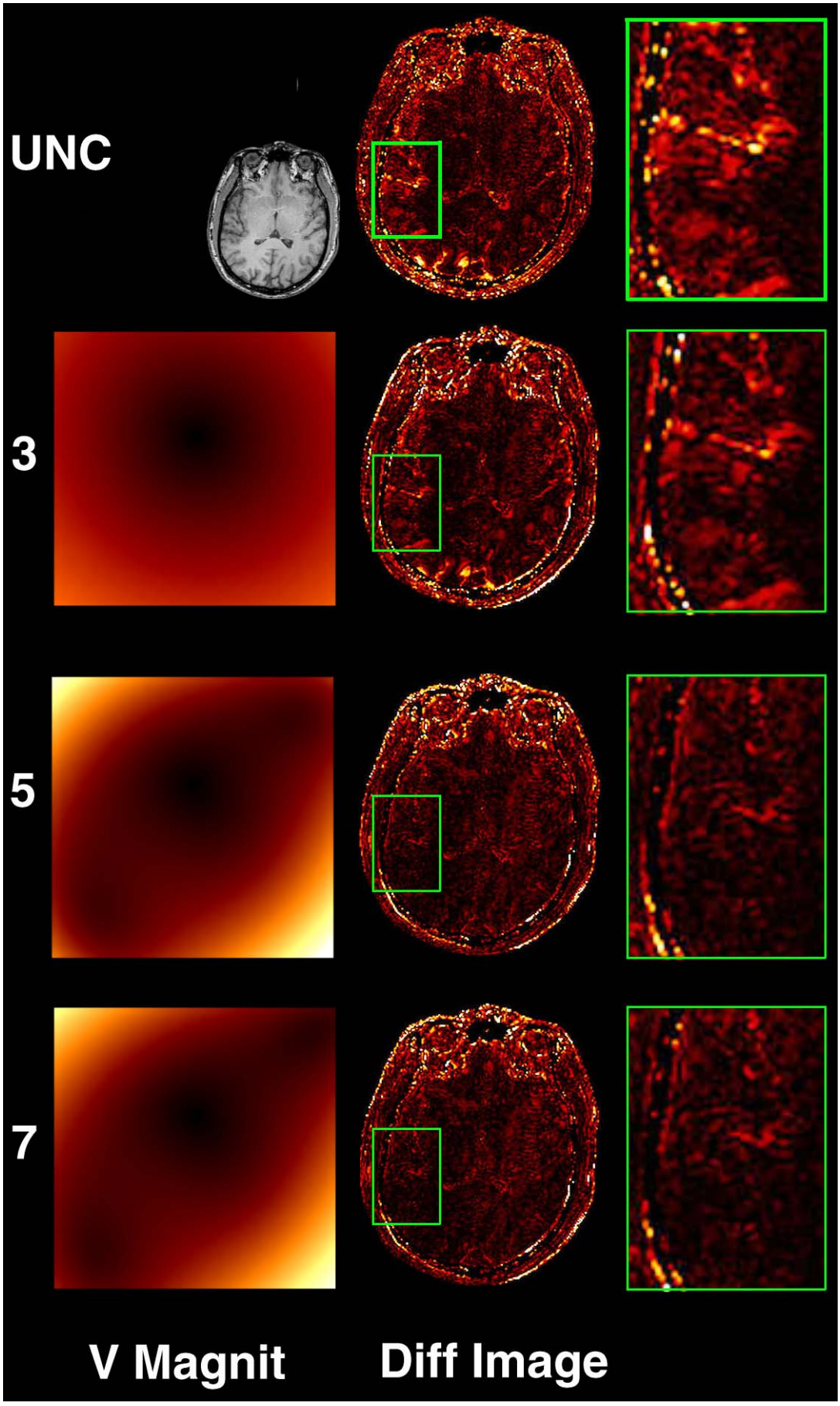
UNC
3
5
7
V Magnit
Diff Image

Figure 6 - Difference maps for uncorrected image and varying orders of correction (to orders 3, 5 and 7). Note the dramatic reduction in cortex anatomic differences in the corrected images as compared to the uncorrected image. A ROI of these changes is given in the right-most column. The left column shows the corresponding vector magnitude image demonstrating the evolution of the inhomogeneity.

To gain a quantitative assessment of the correction schemes effectiveness on anatomical data, a normalised difference (zscore) was calculated between each 0mm and 15mm pair of volumes for each correction level. We chose a normalised difference measure as opposed to root mean squared error (RMSE) or cross correlation as whilst the image pairs have similar intensity profiles, they may differ in mean and standard deviation. Such differences often adversely affect simple measures of similarity. Normalised difference (zscore) is defined for two images X and Y as follows:

$$zscore = \frac{\sum_{i=0}^{n} \left| \left(\frac{x_i - \bar{x}}{\hat{x}} \right) - \left(\frac{y_i - \bar{y}}{\hat{y}} \right) \right|}{n} \qquad [15]$$

Where x_i is a sample from an image, $\bar{x}$ the image mean and $\hat{x}$ the image standard deviation. The resulting z-scores are shown in Figure 7. The correction scheme shows incremental improvement when terms from the harmonic expansion are used to the 6th order, adding the 7th order terms in this case has slightly degraded performance.

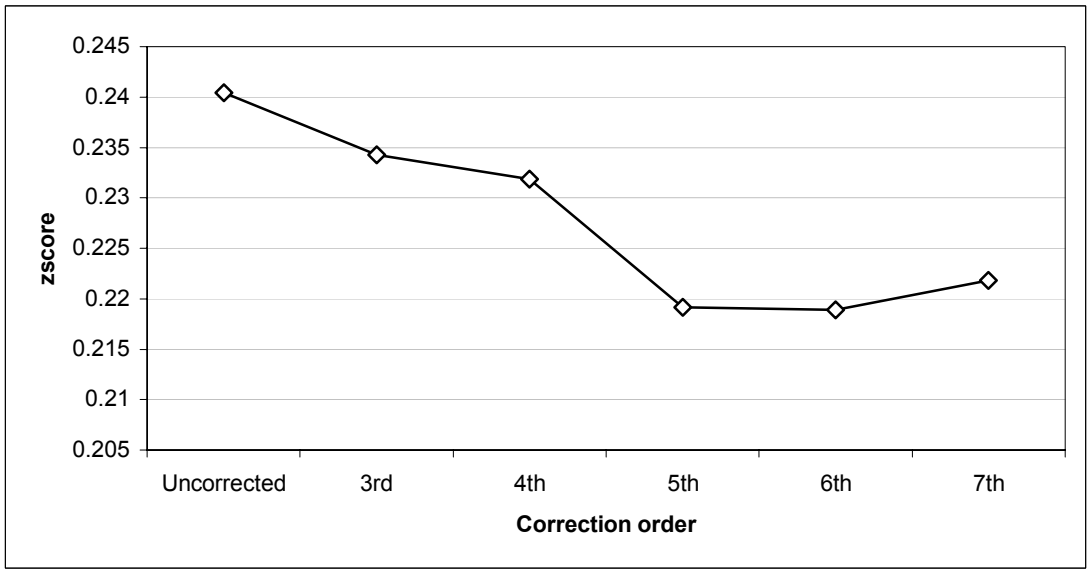

Figure 7 - Z-score error measure vs. Correction order levels.

Discussion

Image distortions induced by gradient non-linearity are a serious problem for the generation of volumetric images using high-speed gradient sets. Although it might be possible to correct such

distortions using translation, warping, and twisting matrices, such approaches are empirical. In this paper, we have demonstrated an image correction technique that quantifies gradient field impurities using spherical harmonics. It should be noted that it is assumed that any extra shimming required for image generation in an initially shimmed magnet are much smaller than the gross in-homogeneities in the gradient field.

A qualification: the image correction techniques outlined above are applicable to correcting image distortions arising from 3D acquisitions using phase encoding in the slice direction. This method is of limited utility to 2D data, as during the slice formation a non-linear gradient field will influence which spins are excited and whether these spins belong in the slice of interest. This problem needs to be resolved to provide a complete distortion correction method.

The anatomical results whilst sufficient to demonstrate the utility of the method are not optimal, this is apparent in the degradation of correction performance when using a 7^{th} order solution. This is due primarily to two reasons. Firstly, the initial measurement of the gradient field was in X and Z only, Y was assumed to be the same as X. Subsequently the data used in the correction scheme will only suffice to a certain level. Secondly, the metric used for image comparison (total z-score difference) whilst largely immune to image intensity scaling problems is not immune to B1 inhomogeneity.

As noted above, a spherical harmonic deconvolution of a Siemens gradient set was carried out at 4T. It is assumed that impurities are present to some extent in all gradients. As such, if this method is used routinely, gradients for a given scanner should be mapped and the corresponding variables stored in a table similar to Table 1. A discrete solution at the desired resolution can then be generated and applied on a routine basis to 3D images.

References

1. Bakker CJ, Moerland MA, Bhagwandien R, Beersma R. Analysis of machine-dependent and object-induced geometric distortion in 2DFT MR imaging. Magn Reson Imaging. 1992;10(4):597-608.
2. Chang H, Fitzpatrick JM. A technique for accurate magnetic resonance imaging in the presence of field inhomogeneities. IEEE Trans. Med. Imaging, 11: 319-329, 1992.
3. Chen NK, Wyrwicz AM. Optimized distortion correction technique for echo planar imaging. Magn Reson Med. 2001 Mar;45(3):525-8.
4. Collins DL, Evans AC. Animal: validation and applications of non-linear registration-based segmentation. Int J Pattern Recog and Art Intell, 1997;11:1271-94.
5. Cusack R, Brett M, Osswald K. An evaluation of the use of magnetic field maps to undistort echo-planar images. Neuroimage. 2003 Jan;18(1):127-42.
6. Eccles CD, Crozier S, Westphal M, Doddrell DM. Temporal spherical-harmonic expansion and compensation of eddy-current fields produced by gradient pulses. Journal of Magnetic Resonance, A 103: 135-141, 1993.
7. Fransson A, Andreo P, Potter R. Aspects of MR image distortions in radiotherapy treatment planning. Strahlenther Onkol. 2001 Feb;177(2):59-73.
8. Krieg R, Schreck O. US patent No. 6501273, issued 31st December 2002.
9. Langlois S, Desvignes M, Constans JM, Revenu M. MRI geometric distortion: a simple approach to correcting the effects of non-linear gradient fields. J Magn Reson Imaging. 1999 Jun;9(6):821-31.
10. Liu H, An efficient geometric image distortion correction method for a biplanar planar gradient coil. Magnetic Resonance Materials in Physics, Biology and Medicine, 10: 75-79, 2000.
11. Maurer CR Jr, Aboutanos GB, Dawant BM, Gadamsetty S, Margolin RA, Maciunas RJ, Fitzpatrick JM. Effect of geometrical distortion correction in MR on image registration accuracy. J Comput Assist Tomogr. 1996 Jul-Aug;20(4):666-79.
12. Mizowaki T, Nagata Y, Okajima K, Kokubo M, Negoro Y, Araki N, Hiraoka M. Reproducibility of geometric distortion in magnetic resonance imaging based on phantom studies. Radiother Oncol. 2000 Nov;57(2):237-42.
13. Mizowaki T, Nagata Y, Okajima K, Murata R, Yamamoto M, Kokubo M, Hiraoka M, Abe M.

Development of an MR simulator: experimental verification of geometric distortion and clinical application. Radiology. 1996 Jun;199(3):855-60.

14. Moerland MA, Beersma R, Bhagwandien R, Wijrdeman HK, Bakker CJ. Analysis and correction of geometric distortions in 1.5 T magnetic resonance images for use in radiotherapy treatment planning. Phys Med Biol. 1995 Oct;40(10):1651-4.
15. Schad L, Lott S, Schmitt F, Sturm V, Lorenz WJ. Correction of spatial distortion in MR imaging: a prerequisite for accurate stereotaxy. J Comput Assist Tomogr. 1987 May-Jun;11(3):499-505.
16. Schad LR, Ehricke HH, Wowra B, Layer G, Engenhart R, Kauczor HU, Zabel HJ, Brix G, Lorenz WJ. Correction of spatial distortion in magnetic resonance angiography for radiosurgical treatment planning of cerebral arteriovenous malformations. Magn Reson Imaging. 1992;10(4):609-21.
17. Tanner SF, Finnigan DJ, Khoo VS, Mayles P, Dearnaley DP, Leach MO. Radiotherapy planning of the pelvis using distortion corrected MR images: the removal of system distortions. Phys Med Biol. 2000 Aug;45(8):2117-32.
18. Woo JH, Kim YS, Kim SI. The correction of MR images distortion with phantom studies. Stud Health Technol Inform. 1999;62:388-9.
19. Yu C, Petrovich Z, Apuzzo ML, Luxton G. An image fusion study of the geometric accuracy of magnetic resonance imaging with the Leksell stereotactic localization system. J Appl Clin Med Phys. 2001 Winter;2(1):42-50.
20. Zhu Y, US patent application publication No. US 2002/0093334, pub. Date 18th July 2002.

Table 1. The relative value of the coefficients of the harmonic impurities obtained using a 24-plane plot of a Sonata gradient set interfaced to an Oxford Magnet Technology 4T whole-body magnet. The shimmed field is first mapped and the associated harmonics are subtracted from those generated by the gradients.

Harmonic	Effect of 2mT/m GX	Effect of 2mT/m GZ	Harmonic	Effect of 2mT/m GX	Effect of 2mT/m GZ	Harmonic	Effect of 2mT/m GX	Effect of 2mT/m GZ
a[1][0]	2.763	129.685	b[4][2]	-0.32	-0.04	b[6][1]	0.556	0.314
a[1][1]	142.603	-0.2	b[4][3]	0.051	-0.038	b[6][2]	0.223	-0.002
b[1][1]	-3.03	-0.054	b[4][4]	-0.212	-0.468	b[6][3]	0.042	0.012
a[2][0]	-0.333	0.606	a[5][0]	-0.099	-12.393	b[6][4]	-0.029	-0.016
a[2][1]	0.749	0.009	a[5][1]	-10.861	0.022	b[6][5]	0.02	0.016
a[2][2]	0.063	0.098	a[5][2]	0.035	0.055	b[6][6]	0.014	-0.002
b[2][1]	0.744	0.137	a[5][3]	0.523	-0.049	a[7][0]	0.091	6.245
b[2][2]	1.13	0.019	a[5][4]	-0.019	-0.037	a[7][1]	5.248	-0.023
a[3][0]	-0.496	-13.763	a[5][5]	-0.482	-0.067	a[7][2]	-0.019	-0.022
a[3][1]	-16.481	-0.023	b[5][1]	0.263	-0.047	a[7][3]	-0.077	0.009
a[3][2]	0.042	-0.011	b[5][2]	0.067	-0.031	a[7][4]	0.005	-0.011
a[3][3]	0.07	-0.046	b[5][3]	-0.023	-0.012	a[7][5]	-0.092	-0.031
b[3][1]	0.424	0.012	b[5][4]	-0.008	-0.006	a[7][6]	-0.004	0.005
b[3][2]	-0.024	0.018	b[5][5]	-0.017	-0.017	a[7][7]	0.111	-0.054
b[3][3]	0.055	-0.014	a[6][0]	0.126	-0.738	b[7][1]	-0.117	-0.009
a[4][0]	-0.143	0.882	a[6][1]	-0.536	-0.04	b[7][2]	-0.021	-0.014
a[4][1]	0.742	0.164	a[6][2]	-0.03	-0.005	b[7][3]	0.021	0.007
a[4][2]	-0.009	0.002	a[6][3]	-0.044	0.003	b[7][4]	0.009	0.001
a[4][3]	-0.028	-0.024	a[6][4]	-0.038	0.002	b[7][5]	-0.005	-0.003
a[4][4]	-0.111	0.014	a[6][5]	0.017	0.007	b[7][6]	-0.009	-0.001
b[4][1]	-0.072	-0.566	a[6][6]	-0.045	-0.004	b[7][7]	0.015	0.004